A high-resolution fuel type mapping procedure based on satellite imagery and neural networks: Updating fuel maps for wildfire simulators

Marcos López-De-Castro [a, *], Diego Prieto-Herráez [b], María Isabel Asensio-Sevilla [b, c], Gianni Pagnini [a, d]

[a] *BCAM-Basque Center for Applied Mathematics, Alameda de Mazarredo 14, Bilbao, 48009, Basque Country, Spain*
[b] *Applied Mathematics Department, Universidad de Salamanca, Casas del Parque 2, Salamanca, 37008, Castilla y Leon, Spain*
[c] *Fundamental Physics and Mathematics University Institute, Casas del Parque 1, Salamanca, 37008, Castilla y Leon, Spain*
[d] *Ikerbasque-Basque Foundation for Science, Plaza Euskadi 5, Bilbao, 48009, Basque Country, Spain*

ARTICLE INFO

ABSTRACT

A major limitation in the simulation of forest fires involves the proper characterization of the surface vegetation over the study area, based on land cover maps. Unfortunately, these maps may be outdated, with areas where vegetation is either not documented or inaccurately portrayed. These limitations may impair the predictions of wildfire simulators or the design of risk maps and prevention plans. This study proposes a complete procedure for fuel type classification using satellite imagery and fully-connected neural networks. Specifically, our work is based on pixel-based processing cells, generating high-resolution maps. The field study is located in the Northeast of Castilla y León, a central Spanish region, and the Rothermel criteria was followed for the fuel classification. The results record an accuracy of close to 78% on the test sets for the two studied settings, improving on the results reported in previous studies and ratifying the robustness of our approach. Additionally, the confusion matrix analysis and the per-class statistics computed confirm good reliability for all fuel types in a cross-validation framework. The predicted maps can be used on wildfire simulators through GIS tools.

1. Introduction

The impact of climate change is increasing all over the world (IPCC et al., 2021), making weather phenomena more extreme, affecting plant and forest cover. Wildfires are no exception, becoming more frequent and destructive each year (Moreira et al., 2011; Aponte et al., 2016), although they are admittedly part of the natural dynamics of ecosystems (Keeley et al., 2011). They are also, nonetheless, one of their main threats, critically affecting the environment, biodiversity, and socioeconomic activities (Stephenson et al., 2013). It is crucial to predict the behavior of wildfires in order to combat them, as this helps us to develop the most appropriate strategies. Several modelling approaches have therefore been developed to tackle the problems involved in wildfire simulation (Sullivan, 2009a,b,c). However, developing a model to describe a real-world wildfire and its effects (Prieto-Herráez et al., 2017; Trucchia et al., 2019; Asensio et al., 2020b) requires accurate data on the characteristics of the fuel to be burnt (Ferraz et al., 2009; Stavros et al., 2018), which can be incorporated into the model (Asensio et al., 2020a). Fuel data are obtained from land cover maps (Anderson, 1982). Unfortunately, these maps may have certain shortcomings such as their non-availability, lack of updating, or in-

* Corresponding author.
E-mail address: malopez@bcamath.org (M. López-De-Castro).

complete nature. These disadvantages became evident in countries frequently affected by wildfires, as is the case of Spain. According to the annual report of the European Forest Fire Information System (EFFIS) (European Commission. Joint Research Centre et al., 2021), wildfires pose a present and future threat to forest areas. In Europe, the countries located in the Mediterranean basin are those that register the most of fires; in particular, Spain records the largest area affected by forest fires in recent decades. According to the Spanish Ministry for Ecological Transition and Demographic Challenge (2022), between 2000 and 2021 a total of 24, 142.03 km^2 were burnt in Spain, with 2012 being the worst year with 2, 189.57 km^2. The number of fires amounted to 113, 481 (surface burnt greater than 0.01 km^2), and the majority of them were provoked (56%).

This study therefore proposes an operational solution based on remote sensing technology and machine learning to deal with these issues (Jain et al., 2020), allowing the drafting of updated fuel type maps through multispectral satellite data and neural networks following the Rothermel classification (Rothermel, 1972). In particular, the procedure proposed here has two fundamental parts. The first step involves data processing, and the second one considers the actual prediction. Accordingly, we have assigned each pixel in the satellite imagery its corresponding fuel type, and then we have used an artificial neural network architecture to build a pixel-based classifier.

Neural networks can tackle non-linear problems, making them a suitable tool for fuel type prediction. The most commonly used neural networks are the so-called Multilayer Perceptrons (MLPs) (Atkinson and Tatnall, 1997) and Convolutional Neural Networks (CNNs) (Lecun et al., 1998). The standard procedure in image classification is to use CNN. However, the objective here is to develop a procedure that will allow us to use satellite data to predict fuel maps with a one-pixel resolution large enough areas to cover the extension of a major wildfire. Consequently, we have chosen a pixel-based approach, which has already been explored by other scholars for remote sensing applications (Dean and Smith, 2003; Kamal and Phinn, 2011; Myint et al., 2011; Singh and Tyagi, 2021). It is based on considering solely each one of the pixels that compose the satellite image and estimating their associated fuel type through the intensity of each pixel's component channel spectrum. MLPs are more suitable for the classification of raster inputs, so we have chosen this neural network architecture to build our classifier. Interesting studies have recently proposed mixing both MLP and CNN architectures for classifying land uses (Zhang et al., 2019; Ashiagbor et al., 2020), with promising results. It is well known that some indices were developed to highlight some features in the spectral data collections. Following this idea, we have considered a second dataset adding some spectral indices that we contend could help the classifier to tackle the problem (i.e. NDVI, GNDVI, EVI, AVI, SAVI, GCI, ARVI, SIPI, NDMI, BSI, NDWI, and NDSI). Finally, we have compared the performance for both cases, with and without the spectral indices, and predicted the annual fuel maps for the studied area for 2013, 2015, and 2017. The comparison of the overall and per-class statistics will confirm if these indices are beneficial for classification purposes, or if the original data collected from the bands is enough.

The paper is organized as follows. Relevant related work are exposed in Section 2. Section 3 presents the main characteristics of the area of interest (AOI) and the data sources used. Section 4 explains the proposed procedure. The results are analyzed in Section 5, and fuel type maps for the AOI are shown. Section 6 discusses the results and the predicted maps. The limitations of the proposed procedure are also exposed as well as future research is suggested. Finally, Section 7 presents the study's conclusions.

2. Remote sensing, machine learning, and wildfires: an overview

The use of remote sensing tools in wildfire research has been an intensive research field in the recent decades (Szpakowski and Jensen, 2019). In particular, previous studies have explored fuel type mapping through spectral imagery from different points of view. Riaño et al. (2002) have used maximum likelihood algorithms to classify fuel types in a Spanish region using *Landsat* TM spectral data. Subsequent studies include LIDAR combined with multispectral data. García et al. (2011) have trained a SVM to classify fuel types in Spain, Ruiz et al. (2018) have compared C4.5 decision trees, random forest (RF), k-Nearest Neighbour(kNN) and Support Vector Machine (SVM) classifiers to measure their performance in fuel type classifications, and Huesca et al. (2019) have estimated vegetation structural data with an RF algorithm. Ruiz et al. (2018) report that using only spectral imagery recorded an overall accuracy of under 70%. We refer the reader to Gale et al. (2021) for an extended review of the literature in remote sensing applied to fire fuel in forest environments, including fuel type mapping studies, over the last decade.

As far as we know, the most recent study with the same aim as our own research has been conducted by Domingo et al. (2020). Their study describes the fuel type mapping of three forests in the Spain's Mediterranean regions that were affected by wildfires in 1994 over an area of 2, 023.1 km^2. Specifically, their study classifies seven different fuel types following cross-validation and stratified random sampling strategies, achieving an overall accuracy of 59% in the validation phase with a SVM with radial kernel, spectral data from Sentinel 2, and a low-density Airborne Laser Scanner. However, one of the approaches followed in their study involves a classification using only spectral data, (i.e., four Sentinel 2 indexes and a NIR band), obtaining an overall accuracy of 0.38 for a SVM with linear kernel and 0.18 with an RF algorithm. Another similar study, conducted by Marino et al. (2016), proposes the generation of high-resolution fuel maps of the Canary Islands (3, 678 km^2). The authors achieved an accuracy of 70% and 82% for the two data sets, corresponding to two different fuel type classifications. The first one is a general fuel type classification for Spain, and records an accuracy of 82%, albeit with a kappa score of 0.77. The second data set comes from a specific fuel type classification for the Canary Islands, recording 70% accuracy and a kappa score of 0.67. An RF algorithm was used as classifier, and the possibility of a cross-validation procedure was not considered.

3. Materials

3.1. Fuel types

The proposed AOI is located in the Spanish region of Castilla y León (see Fig. 1), with diverse types of vegetation. The regional government, *Junta de Castilla y León* (JCyL), in collaboration with the company (Tragsatec, 2022), drew up in 2012 a regional fuel map, applying Rothermel criteria adapted by Spain's environmental agency - ICONA (1987). The fuel map provided by *Tragsatec* considers nine different types of fuels plus an additional one that includes non-flammable areas. The temporary vestiges of forestry operations are not included because of their temporal nature and the lack of data for their identification. In this study, we use the fuel type map drawn up by *Tragsatec*, provided as a shapefile, as the reference data for training the classifier.

Table 1 describe the characteristics of the fuel types.

Fig. 1. Location of Spain's Castilla y León region (red). (For interpretation of the references to colour in this figure legend, the reader is referred to the Web version of this article.)

Table 1
Fuel types considered in this work.

Group	Fuel type	Description
Pasture	1	Thin, dry, low pasture. Land is fully covered. 1/3 of the land is covered by scrub or woodland.
	2	Pasture with scrub or light woodland covering between 1/3 and 2/3 of the surface.
	3	Thick and tall (Height $\leq 1\ m$), such as cereal crops.
Scrub	4	Dense scrub or woodland (2 m height). The fire spreads quickly over the scrub.
	5	Low dense scrub. (Height $\leq 0.6\ m$).
	6	Older scrub than in type 5, between 0.6 and 1.2 m high. More flammable than model 5.
	7	Flammable scrub from 0.6 to 2 m high. The fire spreads under the wooded area.
Leaf litter	8	Leaf litter in dense coniferous forest. The scrub makes a compact layer and the fire is not very intense.
	9	Leaf litter in dense coniferous forest, loosely packed spongy layer with intermediate air. Less dense than type 8.
–	10	Omitted areas: Lakes, roads, villages, etc.

3.2. Attributes

3.2.1. Spectral inputs

Our main data source is the multispectral imagery provided by *Landsat 7* and obtained from *Google Earth Engine* (GEE) (Gorelick et al., 2017) between January 1, 2012 and December 31, 2012. These dates coincide with the period when the reference fuel type map was produced. We have computed the mean intensity of the pixels for the same ground point in the different images taken during the study period to create suitable raster data for the proposed procedure's input. We have chosen imagery from this particular satellite because the data provided are available from July 1999 through to the present. The specific name of the collection used is *USGS Landsat 7 Surface Reflectance Tier 1* (USGS). *Landsat 7* spectral data consist of seven spectral bands with 30 *m* spatial resolution provided by an ETM + device and processed with LEDAPS software (Schmidt et al., 2013) (see Table 2).

On May 31, 2003, the ETM + sensor's Scan Line Corrector (SLC) experienced a catastrophic failure, whereby around 20% of the pixels per scene were not scanned. Since then, several methods have been used to recover *Landsat 7*'s lost pixels (Maxwell et al., 2007; Yin et al., 2017). LEDAPS software provides us with three additional bands to express the quality of the pixels.

In addition, three extra spectral bands have been considered, namely, B01, B02 and B3N from the *ASTER L1T Radiance data set* (NASA, 2015) (see Table 2 for more information). This data set has been collected through the ASTER device, a sensor onboard the *Terra* satellite.

The first two bands have the same wavelength as bands B2 and B3 of the ETM + *Landsat 7* sensor. The main differences involve pixel resolution, which is 15 *m/pixel* for the ASTER products and 30 *m/pixel* for the ETM + ones. These band pixels have been sampled to 30 *m/pixel* in agreement with previous imagery resolution. Band B3N is slightly different from B4 due to the shortest wavelength of the spectrum range. In this case, we have collected data from a previous period - January 1, 2011 to December 31, 2011 – because the GEE data set does not provide information from January 1, 2012 to December 31, 2012 for the AOI.

3.2.2. Physical and terrain data

In addition to pure spectral indices, we have considered both annual daytime and night-time LSTs and topography as inputs for the proposed procedure. The first two data sets (see Table 2) have been obtained from the *MOD11A1 V6* product (Wan et al., 2015) through the GEE tool. This data set was created with the MODIS sensor, onboard the *Terra* satellite. This product's resolution is 1 km/*pixel*, but previous satellite imagery had 30 *m/pixel*, so pixel interpolation has been carried out.

Height information has been obtained from the NASA Digital Elevation Model (NASADEM) the *NASA Digital Elevation Model*, 30 m product (NASA, 2020) through the GEE tool (see Table 2).

3.2.3. Spectral indices

We have used the spectral data provided by the ETM + sensor to compute some of the more relevant spectral indices in the remote sensing studies (see Table 3).

3.3. Area of interest

The proposed AOI in this study is shown in Fig. 2. We consider this study area suitable because of its low urban concentration, the presence of all fuel types, and the complex topography of the terrain (see Fig. 4 - B). Fuel type 10 is not considered in the proposed AOI due to the heterogeneity of the elements labelled within it and, furthermore, features such as roads, urban areas or lakes can be reconstructed in a post-processing step through other data sources (Navarro-Carrión et al., 2021), such as Spain's national topographic bases (IGN, 2016). In addition, the AOI (561.4 km^2) is prone to forest fires, according to the Spanish National Database of Wildfires, the period from 1996 to 2015 recorded 30 wildfires in the AOI, with a total burnt area of 1.6 km^2 (IGN, 2021). Table 4 displays the number of pixels associated with each fuel type.

Table 2

Spectral data considered: *Landsat 7* spectral bands provided by the ETM + sensor and available in GEE as a surface reflectance product, ASTER spectral bands, temperature information obtained from the MODIS sensor, and height data. LST = land surface temperature.

Band name	Wavelength (μm)	Resolution ($m/pixel$)	Band description
B1	0.45–0.52	30	Band 1 (blue).
B2	0.52–0.60	30	Band 2 (green).
B3	0.63–0.69	30	Band 3 (red).
B4	0.77–0.90	30	Band 4 (near infrared).
B5	1.55–1.75	30	Band 5 (shortwave infrared 1).
B6	10.40–12.50	60	Band 6 brightness temperature.
B7	2.08–2.35	30	Band 7 (shortwave infrared 2).
B01	0.52–0.60	15	VNIR_Band1 (visible green/yellow).
B02	0.63–0.69	15	VNIR_Band2 (visible red).
B3N	0.78–0.86	15	VNIR_Band3N (near infrared, nadir pointing).
LST_Day_1 km	–	1,000	Daytime Land Surface Temperature in Kelvin.
LST_Night_1 km	–	1,000	Night-time Land Surface Temperature in Kelvin.
elevation	–	30	Height of the terrain in meters.

Table 3

Mathematical formulation of the spectral indices used in this work. They highlight some of the characteristics of certain vegetation covers. The constants are $G = 2.5$, $l = 1.0$, $C_1 = 6.0$ and $C_2 = 7.5$. SWIR = Short-wave infrared; NIR = Near infrared.

Index	Name	Use	Mathematical formulation	References
NDVI	Normalized Difference Vegetation Index.	To estimate the vegetation's size, quality and growth.	$NDVI = \frac{NIR-RED}{NIR+RED}$	(Tucker, 1979)
GNDVI	Green Normalized Difference Vegetation Index.	To estimate the size, quality and growth of the vegetation and whether it is sensitive to chlorophyll concentration.	$GNDVI = \frac{NIR-GREEN}{NIR+GREEN}$	(Gitelson et al., 1996)
EVI	Enhanced Vegetation Index.	It is useful for detecting a high vegetation density.	$EVI = G \frac{NIR-RED}{NIR+C_1\ RED-C_2\ BLUE+l}$	(Huete et al., 1994)
AVI	Advanced Vegetation Index.	For monitoring changes in crops and forests.	$AVI = (NIR\,(1-RED)\,(NIR-RED))^{\frac{1}{3}}$	(Silleos et al., 2006)
SAVI	Soil Adjusted Vegetation Index.	It is an NDVI correction of the influence of brightness in areas with less density of vegetation.	$SAVI = \frac{NIR-RED}{NIR+RED+l}\,(1+l)$	(Huete, 1988)
GCI	Green Chlorophyll Index.	To estimate the chlorophyll content of the leaves of different types of plants and crops.	$GCI = \frac{NIR}{GREEN} - 1$	(Gitelson et al., 2005)
ARVI	Atmospherically Resistant Vegetation Index.	It is sensitive to atmospheric factors.	$ARVI = \frac{NIR-2\ RED+BLUE}{NIR+2\ RED+BLUE}$	(Bannari et al., 1995)
SIPI	Structure Insensitive Pigment Index.	To analyze vegetation with the canopy's variable structure.	$SIPI = \frac{NIR-BLUE}{NIR-RED}$	(Pu et al., 2008)
NDMI	Normalized Difference Moisture Index.	NDMI determines the plant water content of the vegetation.	$NDMI = \frac{NIR-SWIR}{NIR+SWIR}$	(Cibula et al., 1992)
BSI	Bare Soil Index.	It quantifies the soil's mineral composition.	$BSI = \frac{(RED+SWIR)-(NIR+BLUE)}{(RED+SWIR)+(NIR+BLUE)}$	(Chen et al., 2004)
NDWI	Normalized Difference Water Index.	For measuring the plant water content or the soil level of moisture saturation.	$NDWI = \frac{GREEN-NIR}{GREEN+NIR}$	(Gao, 1996)
NDSI	Normalized Difference Snow Index.	To detect the presence of snow in a given area	$NDSI = \frac{GREEN-SWIR}{GREEN+SWIR}$	(Rogers Kearney, 2004)

Fig. 2. Chosen AOI. The satellite image displays the spectral bands B3 (Red), B2 (Green), and B1 (Blue); taken from *Landsat 7* (ETM + device). (For interpretation of the references to colour in this figure legend, the reader is referred to the Web version of this article.)

Table 4

Number of samples of each class in the data set and their percentages over the total amount.

Fuel type	Number of samples	%
1	58,922	7.07
2	52,795	6.33
3	91,700	11.00
4	189,964	22.78
5	62,161	7.45
6	111,023	13.31
7	97,392	11.68
8	99,308	11.91
9	42,777	5.13
10	27,812	3.34

4. Methodology

This section describes the different steps in the proposed procedure (see Fig. 3).

4.1. Image processing

The pixel-based processing approach has been used. The algorithm developed to create the data set, input 1, operates as follows:

1. Identify the area we are interested in for updating its fuel distribution and data gathering. In order to create an adequate data set, this area should contain as many fuel types as possible. We therefore recommend that the chosen area should have a
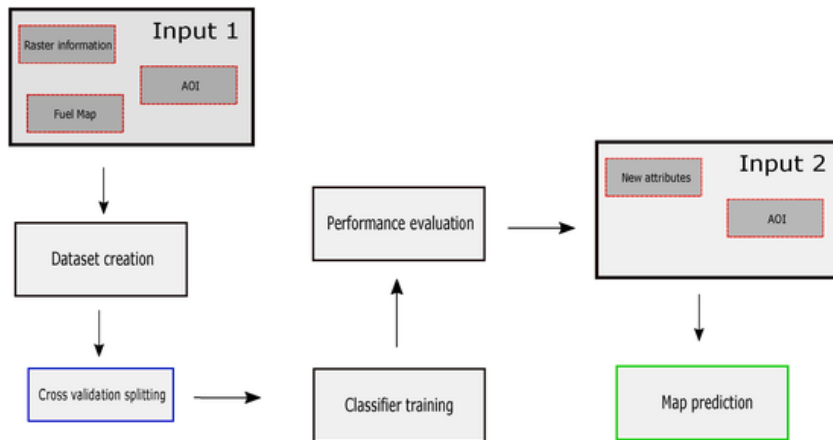
Fig. 3. General scheme of the proposed procedure.

suitable surface extension in which all the fuel types are included, taking into account the rising computational cost of training and processing the results.

2. The data then need to be converted into the same format and reference system (e.g., *World Geodetic System 1984* - WGS 84).

3. We then intersect the full fuel type map of reference with the AOI. This point will allow us to associate the raster data with the fuel type map.

4. The following step involves extracting areas with the same fuel type from the raster data. Both illustrative examples are provided in Fig. 4: in the fuel type map, the light blue area and the orange area inside the black squares are zones in which fuel type 4 and 8 are expected. The raster data are then cut according to the shapefile of this enclave. Pixels outside the cut area are labelled as non-data flag. At this point, we assign each pixel the fuel type present in the area. In the previous example, all the pixels inside the two areas are labelled as fuel types 4 and 8. The above process is carried out for all the features in the shapefile with fuel type information, except for those under 900 m^2 because of the resolution of the satellite imagery used.

5. At this point, we create a table with all the data sets and data on pixel intensities are normalized.

6. Finally, we create new attributes for each pixel, corresponding to the artificial spectral indices described in Section 3.2.3.

Each fuel type is associated with 28 potential attributes; some are provided by satellite spectra, and others are built from them.

4.2. Sample analysis

Table 4 shows the percentage of each class in the AOI and the highly unbalanced data set created from our AOI, where some classes are more than four times more common than others. This situation may lead to a scenario in which the classifier learns to identify the majority classes fairly well, while unable to recognize the minority ones, weakening the model's generalization capacity (Waske et al., 2009). We have used the stratified random sampling strategy to solve the data set's problem of imbalance. This decision is informed by the simplicity of the technique, as well as by its verified effectiveness (Marino et al., 2016; Domingo et al., 2020). We have implemented the technique through a random choice of a number of samples equal to the number in the data set's minority class, maintaining the same class distribution in each subset. This has provided a balanced data set. However, this may mean that the training data are not representative of our AOI. The training period has therefore involved a fivefold cross-validation strategy for the neural network. There are two reasons for implementing this strategy: first, if varying the training and validation sets does not cause major discrepancies in the results, it means the samples are representative of the AOI. Second, this division of the data set enables us to study the classifier's performance for different sets of the same area, providing us with a more realistic picture.

4.3. Classifier model

The relationship between attributes and their associated fuel type may be highly non-linear or even unknown, so neural networks are a suitable tool for building an appropriate classifier. The network topology considered here consists of a fully connected four-hidden-layered MLP network. To learn the features properly, the learning rate, batch-size, and the maximum number of epochs were set as 10^{-5}, 32 and 1500, respectively. The neurons inside each layer contain *ReLU* activation functions (Nair and Hinton, 2010; Maas et al., 2013), except for the last layer, in which a *softmax* function has been used for the classification. A 30% *dropout* was used in each layer as a regularization method to prevent overfitting (Srivastava et al., 2014). The neural network has been adjusted to minimize the *categorical cross-entropy* function between observed and predicted classes. *Adam* optimization has also been used (Kingma and Ba, 2017). Considering the cross-validation strategy, the original data set will be split into five different parts, all with the same size and the same number of samples for each class. In each step, 20% of the samples are used for testing purposes, 20% for validation, and 60% for training, with the test set always being one of the five subsets created. Specifically, the data set is divided into five subsets to ensure that the training set has enough samples, and test sets are also representative of the total number of samples.
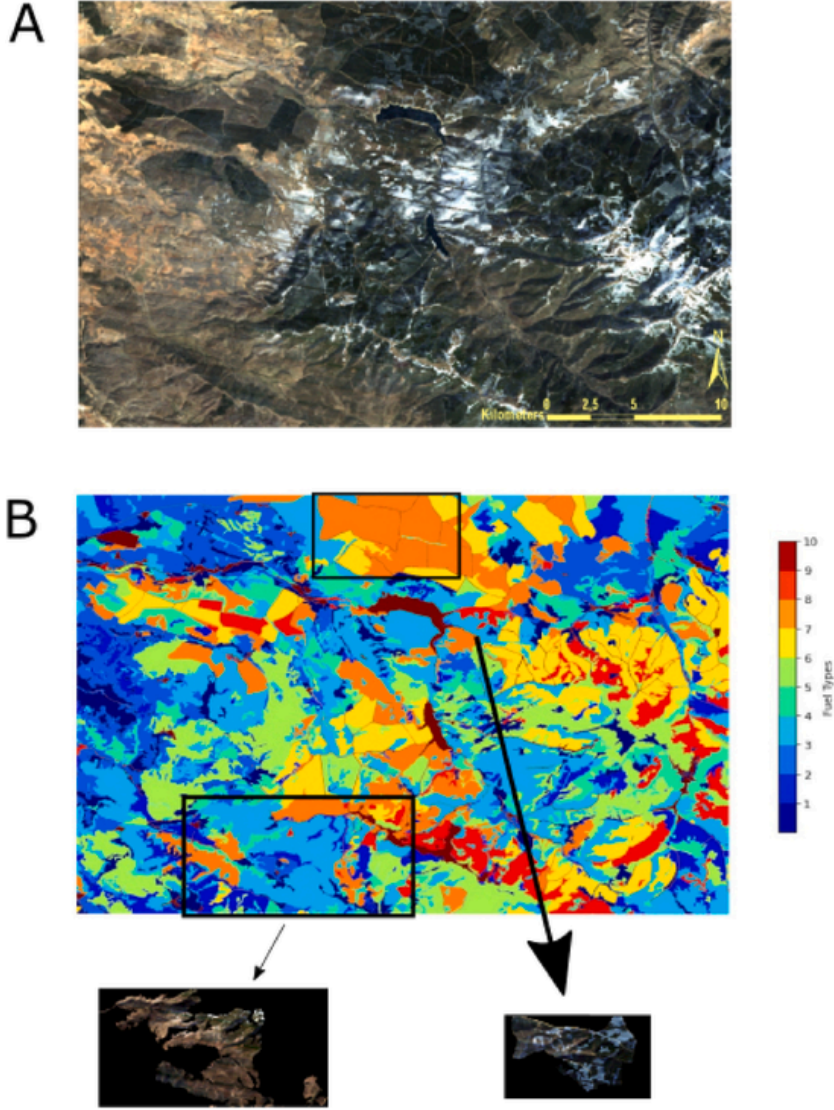
Fig. 4. Cut area example. Figure A shows the satellite image of the AOI (spectral bands B3 (Red), B2 (Green), and B1 (Blue); taken from *Landsat 7*, ETM + device). Figure B shows the reference fuel map of the AOI. This map reveals the complex distribution of the fuel types. We cut the pixels in the original raster that belong to a labelled area and identify them with the corresponding fuel. The black rectangles show a raster cut following the illustrative examples described in step number 4. (For interpretation of the references to colour in this figure legend, the reader is referred to the Web version of this article.)

4.4. Performance evaluation

The evaluation method is a crucial factor for the performance of the proposed procedure. Our classifier is multiclass, so we have used three overall statistical measures, namely, Accuracy, Cohen's kappa, and the Matthews correlation coefficient. Accuracy is computed as the ratio of samples correctly classified over the total number of samples (Zhang et al., 2021):

$$\text{Acc} = \frac{\text{TP} + \text{TN}}{\text{TP} + \text{TN} + \text{FP} + \text{FN}}, \tag{1}$$

where TP is the true positive number of samples classified, TN is the true negative number of samples classified, FP is the false positive number of samples classified, and FN is the false positive number of samples classified. Cohen's kappa index rate reflects the classifier's reliability (Cohen, 1960):

$$\kappa = \frac{P_o - P_e}{1 - P_e}, \tag{2}$$

where P_o is the observed agreement ratio, defined as the probability of agreement between the predicted and true label values:

$$P_o = \text{TP} + \text{TN}, \tag{3}$$

and P_e is the probability that true and false values agree by chance:

$$P_e = (\text{TP} + \text{FN})(\text{TP} + \text{FP}) + (\text{FP} + \text{TN})(\text{FN} + \text{TN}). \tag{4}$$

The kappa value range falls between 0 and 1, where 0 means no difference between random choice and the classified sample, and 1 means perfect agreement between classified and observed samples. The range between 0.81 and 1 is commonly considered almost perfect (Landis and Koch, 1977). The Matthews correlation coefficient was first introduced for multiclass classification (Gorodkin, 2004), and is generally regarded as a balanced measure that represents the correlation between reference and predicted values. It can also be used even when working with a highly unbalanced data set. X and Y are two matrices with N rows, where N is equal to the number of samples, and K columns, where K is equal to the number of classes. Matrix X is defined as follows: $X_{ik} = 1$ if i sample is predicted as k class, and 0 otherwise. Matrix Y is defined as follows: $Y_{ik} = 1$ if i sample belongs to k class, and 0 otherwise. The covariance function between X and Y can be stated as follows:

$$\text{COV}(X, Y) = \frac{1}{K} \sum_{i=1}^{N} \sum_{k=1}^{K} \left(X_{ik} - \bar{X}_k \right) \left(Y_{ik} - \bar{Y}_k \right), \tag{5}$$

where $\bar{X}_k = (1/N) \sum_{i=1}^{N} X_{ik}$ and $\bar{Y}_k = (1/N) \sum_{i=1}^{N} Y_{ik}$. The Matthews correlation coefficient for multiclass classification is defined as:

$$\text{MMC} = \frac{\text{COV}(X, Y)}{\sqrt{\text{COV}(X, X)\text{COV}(Y, Y)}} \tag{6}$$

The evaluation metrics explained above were implemented to characterize the classifier's overall performance, although we can build a confusion matrix to discover its per-class statistics. This matrix allows us to use typical binary classification metrics as per-class statistics. These metrics will be precision, recall, and F-1 score (Zhang et al., 2021). Precision gives us the proportion of predicted positives that are truly positive (Eq. (7)):

$$\text{Precision} = \frac{\text{TP}}{\text{FP} + \text{TP}}. \tag{7}$$

This metric is a good way of discovering whether the classifier is sensitive to false positives. Recall, also known as sensitivity, provides the proportion of positives that are correctly classified (Eq. (8)):

$$\text{Recall} = \frac{\text{TP}}{\text{FN} + \text{TP}}. \tag{8}$$

A good recall score means few false negatives. Finally, the F-1 score is the harmonic mean between precision and recall (Eq. (9)):

$$\text{F1} = 2 \frac{\text{Precision} \times \text{Recall}}{\text{Precision} + \text{Recall}}. \tag{9}$$

5. Results

The performance of the proposed procedure was investigated in two settings. The first one used the attributes corresponding to the pure spectral information obtained from satellite imagery. The second case included the spectral indices described in Table 3. Fuel type 10 was not considered in either case because it represents land cover features that can be characterized by other data sources. In particular, this (i) avoids one source of error, which is inherent to any classification procedure, (ii) the lower the samples employed the faster the training period (iii) the classifier can focus on the rest of the fuel classes, increasing its performance.

For the first case, the overall scores for the fivefold cross-validation steps are presented in Table 5. The results confirm a good predictive ability for the different cross-validation steps, meaning that the training data used in each step are representative of the AOI. The average time to train a subset within this scenario was 9 h and 47 min. Table 5 shows that the best statistics were recorded by subset 4 (78.80% for accuracy, 76.15% for Cohen's kappa, and 76.17% for the Mathews coefficient). It is clear that the classifier used

Table 5
Overall cross-validation scores.

Fold	Accuracy	Cohen	Matthews
1	78.60%	75.93%	75.95%
2	78.78%	76.13%	76.15%
3	78.75%	76.10%	76.12%
4	78.80%	76.15%	76.17%
5	78.79%	76.14%	76.16%

to make the predictions is the one with the better overall statistics in the cross-validation process, so in the remainder of this subsection we focus solely on the results of cross-validation subset 4 for the analysis.

Fig. 5 presents the confusion matrix for the test set in the cross-validation subset 4. Based on these results, we have computed the per-class statistics, which give us a more detailed view of the classifier's performance. The worst result is obtained for the predictions of fuel type 4. Specifically for this class, the recall metric had a score of 0.61, which means that 39% of the samples the classifier predicts as a fuel type other than 4 are in fact type 4. The confusion matrix reveals that fuel type 4 tends to be predicted as type 8. Both fuel types are labelled as areas of dense vegetated, which may explain the difficulties in distinguishing between them. In turn, the classifier is clearly able to recognize samples belonging to fuel type 9. In all cases, there are far fewer wrongly classified samples than those classified correctly in an order of magnitude.

For the second case, we have studied the same classifier scheme, but with 28 attributes; that is, using both pure spectral data and spectral indices. The average time for training a subset within this scenario was 21 h and 8 min, which is more than twice the first scenario. The overall scores for this scenario are featured in Table 7. The results are close to those obtained in the first scenario. Better scores are again achieved during cross-validation step number four (77.78% for accuracy, 74.99% for Cohen's kappa, and 75.01% for the Mathews coefficient).

Fig. 6 shows the computed confusion matrix that allows us to check our classifier's performance for the different types of fuels considered. As expected, most of the samples are on the diagonal of the matrix. The same patterns as in the first case are observed. Finally, Table 8 shows the local scores derived from the confusion matrix. The best scores were recorded for fuel type 9, and the worst for fuel type 4, which is in agreement with the results shown in the first case. The distribution of the best scores in Table 6 is also observed in Table 8.

5.1. Prediction fuel type maps

The high-resolution fuel type maps presented in Figs. 7 and 8 are the annual estimations for 2012, 2013, 2015, and 2017, respectively, with the neural network trained within the first and second case respectively. The spectral data for each year were collected from GEE in the same way as the training data. In both cases, we have used the neural network that provided the best results during the cross-validation phase. The reason for applying the model to 2012 is solely for illustrative purposes, as it is the year in which the reference fuel map was produced. We should note that some of the estimated data were present in the training data set, but it is also the period in which we can see how similar our estimation is compared to the reference scenario (see Fig. 7A, 8 A and 4B). Specifically, the satellite imagery of the AOI contains 833, 854 potential samples, but due to the stratified random sampling strategy, only 384, 993 (46% of the total) were used in the cross-validation phase. In addition, given that the cross-validation strategy uses five folds, and we are using the neural network with better scores to make the predictions, compounded by the fact that the neural network uses only 60% of the data set for training purposes during the cross-validation phase, only 27% of the pixels to be predicted in Fig. 7A and 8A have previously been seen by the neural network. Therefore, the close similarity between the maps estimated for 2012 and the reference map, and between both estimated maps, is a further argument that supports the results and the approach chosen.

Regarding the maps for 2013, see Fig. 7B and 8B, a fuel type variation is predicted for those years. Specifically, the first scenario records a major reduction in the pixels associated with fuel types 4 and 9. In addition, there is also a drop in the pixel density associated with fuel types 5 and 6 in the north-western area of the predicted map. Both maps show a considerable increase in fuel type 1 on the eastern side, although the map using spectral indices increases the pixel density associated with this type of fuel. There is good
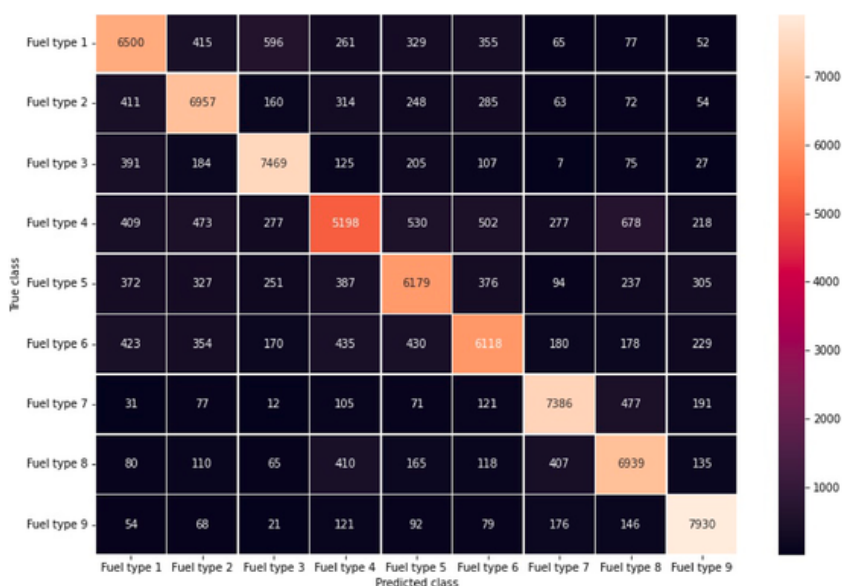

Fig. 5. Confusion matrix with the predictions of the test set in fold number 4. Test set samples were not seen by the classifier in previous stages.

Fig. 6. Confusion matrix with the predictions of the test set in fold four for the second case. The classifier did not see test set samples in previous stages.

Table 6
Metrics for the per-class classification of fold number 4.

Fuel type	Precision	Recall	F-1 Score
1	0.75	0.75	0.75
2	0.78	0.81	0.79
3	0.83	0.87	0.85
4	0.71	0.61	0.65
5	0.75	0.72	0.74
6	0.76	0.72	0.74
7	0.85	0.87	0.86
8	0.78	0.82	0.80
9	0.87	0.91	0.89
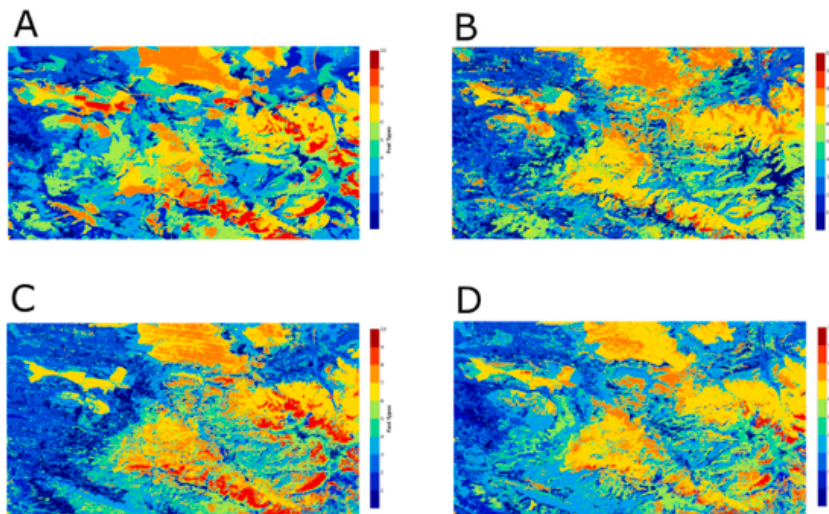
Fig. 7. Predicted fuel map of the AOI for 2012 (Fig. A), 2013 (Fig. B), 2015 (Fig. C), and 2017 (Fig. D) with the neural network trained within the first case.
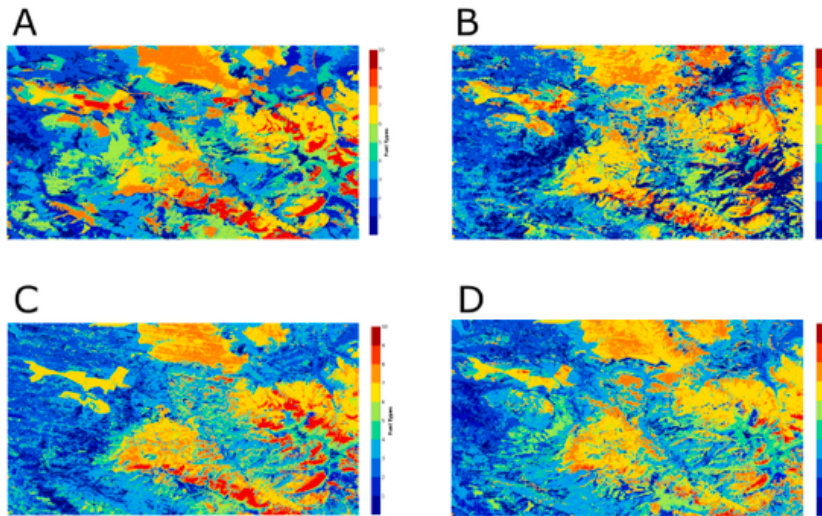
Fig. 8. Predicted fuel map of the AOI for 2012 (Fig. A), 2013 (Fig. B), 2015 (Fig. C), and 2017 (Fig. D) with the neural network trained within the second case.

agreement between the predictions of the fuel type map for 2015 (see Fig. 7C and 8C). Note should be taken of the reappearance of fuel type 9, as its presence in the two previous years had been residual. Finally, the maps associated with 2017 (see Fig. 7 D and 8D) show how fuel type 9 again decreases, suggesting a possible oscillatory dynamic for this fuel type over time. There is also an increase in the density associated with fuel type 4, as well as an advance of fuel type 6, which corresponds to intermediate scrub areas and may involve areas in which fuel type 5 evolves to type 6 (see Table 1).

6. Discussion of the results

The procedure developed here has a satisfactory prediction capacity according to the results reached in the test sets, maintaining similar overall statistics during the cross-validation. As noted in the preceding section, the predicted maps of the evolution of the fuel type in the AOI clearly agree with each other. Together with the similar performance recorded by the statistics used as validation metrics (see Tables 5 and 7), we may conclude that, in our case, the inclusion of data on spectral indices does not significantly alter the results. This is in agreement with the conclusions reported by Riaño et al. (2002). However, the significant presence of fuel type 1 in the predicted maps within the second scenario for 2013 (Fig. 8 - B) compared to the prediction within the first scenario (Fig. 7 - B) shows that the inclusion of the spectral index can help to clarify the presence of a specific type of fuel. Additional forest fuel data on the AOI are available through the *Spain Forest Map* (Spanish Ministry for Ecological Transition and Demographic Challenge, 2020), drawn up 2007 and 2020, and plotted in Fig. 9. Even though the classification criteria were similar, a direct comparison between reference and predicted maps and the official *Spain Forest Map* should be made with caution, due to the low temporal resolution of the official map,

Table 7
Overall cross-validation scores for the second case.

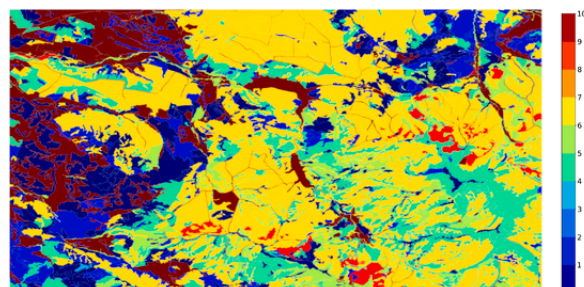| Fold	Accuracy	Cohen	Matthews
1	77.27%	74.43%	74.44%
2	77.51%	74.70%	74.72%
3	77.38%	74.56%	74.57%
4	77.78%	74.99%	75.01%
5	77.02%	74.14%	74.16%

Fig. 9. Spain Forest Map developed by Spanish ministry. In particular, it is represented the forest Map of the studied area.

which shows a high prevalence of fuel type number 7 in detriment to type 8. An increase in fuel type 5 is shown in detriment to fuel type 6. Fuel type 6 is an older scrub than type 5, so it suggests an older date of drafting. The official map also shows far fewer pasture group fuels compared to the increase in omitted fuels over the same areas. The comparison between the official map (see Fig. 9) and the reference map drawn up by *Tragsatec* (see Fig. 4 - B) shows the importance of periodically updating this kind of map.

Tables 6 and 8 present the classification results obtained for each one of the fuel classes considered in the scenarios studied for the best cross-validation step. The differences between them are no more than 3%, which is consistent with the previous paragraph. According to Table 4, fuel type 4 is the most abundant within the AOI; however, it is also the one with the poorest results (see Tables 6 and 8). This is probably due to the high degree of heterogeneity of the intensity spectra corresponding to this class; therefore, the number of samples considered by random sampling may be insufficient for the classifier to achieve its full predictive capacity for this class. The second most abundant fuel type according to Table 4 is number 6. The data show that the network obtains good classification data for this class (Tables 6 and 8), which supports the argument that the bad results obtained by fuel type 4 are due to the particularity and high complexity of its spectra. By contrast, the best results are obtained for fuel types 3, 7 and 9, which correspond to thick open pasture, flammable scrub from 0.6 to 2 m high, and leaf litter in dense coniferous forest with an intermediate air layer, accounting for 10.99%, 11.67%, and 5.13%, respectively, of the total pixels of our AOI. Specifically, the best results are recorded by fuel type 9 for both scenarios considered (see Tables 6 and 8), which is also the least abundant fuel type.

6.1. Limitations and further work

The proposed procedure has certain intrinsic limitations that prompt the need to explore multiple ways of improving its performance in future iterations. An initial one involves an artificially balanced data set with more sophisticated techniques than random sampling. Artificial generative networks are currently being used to increase data set size (Shao et al., 2019), whereby this and similar techniques pave the way for a balanced data set using high quality artificial data based on the original data set. Another shortcoming in the results is the unknown seasonal nature of the training data. This is due to the absence of data on the specific period of the year in which the fuel type map was produced, and it explains why the intensity considered for each pixel is computed as the mean of the pixels in the same position in all the satellite imagery available for the year. We are also aware that one of the major weaknesses of the proposed procedure is the loss of spatial context. This means that pixel attributes have no link to the nearest pixel attributes. Fixing this problem is not easy in the approach taken. Zhang et al. (2019); Ashiagbor et al. (2020) are examples of merging our approach based on MLP with a CNN architecture that considers spatial information in its predictions.

7. Conclusions

This paper has taken the first steps in the formulation of a comprehensive procedure based on neural networks for predicting fuel types that will contribute to the updating of the corresponding maps. The above procedure acquires data from a specific AOI and is designed to be fed with any available satellite data. The pixel-based approach taken allows predicting maps with the same resolution as the input data. The product generated may also be geo-referenced and post-processed through GIS tools for their use in wildfire simulators. Two examples of the application of the proposed procedure have been analyzed: on the one hand, pure spectral data, temperature and height information were used as input attributes. On the other hand, we added some artificial spectral indices, increasing the number of attributes as classifier inputs. Specifically, the map of fuel types for the proposed AOI was drafted in 2012, and it contains ten classes of fuel types one of which has been discarded because the information it contains can be included in a post-processing step. The remote sensing tools used to illustrate the operation of the proposed procedure have been the *Landsat 7* and *Terra* satellites, as they were in service when the fuel map was made. Despite the limitations caused by various failures affecting these satellites' sensors, a good prediction capacity was confirmed in a cross-validation process. In particular, our predictions reached 78% of accuracy in the test phase, with no preference for any fuel type and no 3D data. The global accuracy measured in this study is higher in comparison with the 59% obtained by Domingo et al. (2020) and, specifically, twice compared with the 38% that they reach using only spectral data from Sentinel 2. Therefore, this research supposes a considerable increase in prediction capacity, considering geographical differences and the different fuel type classification used. Moreover, if we compare our results with the research conducted by Marino et al. (2016), our procedure based on neural networks has recorded similar validation scores between both the settings considered, where different attributes were applied to the same AOI, confirming the robustness of the predictions. This study's promising results and the possible work discussed in Section 6 for future iterations of the proposed procedure suggest that it is a

Table 8

Metrics for the per-class classification for fold number 4 within the second case.

Fuel type	Precision	Recall	F-1 Score
1	0.74	0.73	0.74
2	0.76	0.80	0.78
3	0.83	0.87	0.85
4	0.68	0.59	0.63
5	0.73	0.72	0.73
6	0.74	0.71	0.73
7	0.84	0.87	0.86
8	0.79	0.79	0.79
9	0.86	0.91	0.88

strong candidate for complementing any operational wildfire simulator. Finally, it should be noted that despite the general purpose for which the procedure has been designed, no similar studies have been found for the vegetation cover in the AOI.

Authorship

ML, DP, MIA, and GP designed the research. DP and MIA provided the data and ML performed their analysis. ML wrote the manuscript under the supervision of DP. MIA and GP supervised the research. All the authors approved the final version.

Data accessibility

The scripts developed throughout this work can be found here: https://gitlab.bcamath.org/malopez/fuel-type-mapping.git.

Declaration of competing interest

The authors declare that they have no known competing financial interests or personal relationships that could have appeared to influence the work reported in this paper.

Appendix A. Computational resources

The computational resources used in this research were hosted in **HIPATIA** cluster, property of BCAM, and **ATLAS** cluster, property of DIPC (Donostia International Physics Center). The work has been conducted using the Python 3.7 programming language.

References

Anderson, H.E., 1982. In: Aids to Determining Fuel Models for Estimating Fire Behavior. Research Paper INT-122 U.S. Department of Agriculture, Intermountain Forest and Range Experiment Station. https://doi.org/10.2737/INT-GTR-122.

Aponte, C., de Groot, W.J., Wotton, B.M., 2016. Forest fires and climate change: causes, consequences and management options. Int. J. Wildland Fire 25 (8). https://doi.org/10.1071/WFv25n8_FO. . I – II.

Asensio, M., Santos-Martín, T., Álvarez-León, D., Ferragut, L., 2020a. Global sensitivity analysis of fuel-type-dependent input variables of a simplified physical fire spread model. Math. Comput. Simulat. 172 (C), 33–44. https://doi.org/10.1016/j.matcom.2020.01.001.

Asensio, M.I., Ferragut, L., Álvarez, D., Laiz, P., Cascón, J.M., Prieto-Herráez, D., Pagnini, G., 2020b. Phyfire: an online gis-integrated wildfire spread simulation tool based on a semiphysical model. In: Asensio, M., Oliver, A., Sarrate, J. (Eds.), Applied Mathematics for Environmental Problems Chapter 1. Springer Series volume 6 of SEMA SIMAI, pp. 1–20. https://doi.org/10.1007/978-3-030-61795-0_1.

Ashiagbor, G., Forkuo, E.K., Asante, W.A., Acheampong, E., Quaye-Ballard, J.A., Boamah, P., Mohammed, Y., Foli, E., 2020. Pixel-based and object-oriented approaches in segregating cocoa from forest in the Juabeso-Bia landscape of Ghana. Remote Sens. Appl.: Soc. Environ. 19, 100349. https://doi.org/10.1016/j.rsase.2020.100349.

Atkinson, P.M., Tatnall, A.R.L., 1997. Introduction neural networks in remote sensing. Int. J. Rem. Sens. 18, 699–709. https://doi.org/10.1080/014311697218700.

Bannari, A., Morin, D., Bonn, F., Huete, A.R., 1995. A review of vegetation indices. Rem. Sens. Rev. 13 (1–2), 95–120. https://doi.org/10.1080/02757259509532298.

Spanish Ministry for Ecological Transition, Challenge, Demographic, 2020. MFE de máxima actualidad. Comunidad Autónoma de Castilla y León. Available on: https://www.miteco.gob.es/es/cartografia-y-sig/ide/descargas/biodiversidad/mfe_castilla_y_leon.aspx. January, 2022.

Chen, W., Liu, L., Zhang, C., Wang, J., Wang, J., Pan, Y., 2004. Monitoring the seasonal bare soil areas in Beijing using multitemporal TM images. In: IGARSS 2004. 2004 IEEE International Geoscience and Remote Sensing Symposium, vol. 5, pp. 3379–3382. https://doi.org/10.1109/IGARSS.2004.1370024.

Cibula, W.G., Zetka, E.F., Rickman, D.L., 1992. Response of thematic mapper bands to plant water stress. Int. J. Rem. Sens. 13 (10), 1869–1880. https://doi.org/10.1080/01431169208904236.

Cohen, J., 1960. A coefficient of agreement for nominal scales. Educ. Psychol. Meas. 20 (1), 37–46. https://doi.org/10.1177/001316446002000104.

Dean, A.M., Smith, G.M., 2003. An evaluation of per-parcel land cover mapping using maximum likelihood class probabilities. Int. J. Rem. Sens. 24 (14), 2905–2920. https://doi.org/10.1080/01431160210155910.

Domingo, D., de la Riva, J., Lamelas, M.T., García-Martín, A., Ibarra, P., Echeverría, M., Hoffrén, R., 2020. Fuel type classification using airborne laser scanning and Sentinel 2 data in Mediterranean forest affected by wildfires. Rem. Sens. 12, 3660. https://doi.org/10.3390/rs12213660.

Ferraz, A., Bretar, F., Jacquemoud, S., Gonçalves, G., 2009. The role of lidar systems in fuel mapping. INESC: Coimbra, Portugal. https://www.researchgate.net/publication/241475870_The_Role_of_Lidar_Systems_in_Fuel_Mapping.

Gale, M.G., Cary, G.J., Van Dijk, A.I., Yebra, M., 2021. Forest fire fuel through the lens of remote sensing: review of approaches, challenges and future directions in the remote sensing of biotic determinants of fire behaviour. Remote Sens. Environ. 255, 112282. https://doi.org/10.1016/j.rse.2020.112282.

Gao, B., 1996. NDWI - a normalized difference water index for remote sensing of vegetation liquid water from space. Remote Sens. Environ. 58 (3), 257–266. https://doi.org/10.1016/S0034-4257(96)00067-3.

García, M., Riaño, D., Chuvieco, E., Salas, J., Danson, F.M., 2011. Multispectral and LiDAR data fusion for fuel type mapping using support vector machine and decision rules. Remote Sens. Environ. 115, 1369–1379. https://doi.org/10.1016/j.rse.2011.01.017.

Gitelson, A.A., Kaufman, Y.J., Merzlyak, M.N., 1996. Use of a green channel in remote sensing of global vegetation from EOS-MODIS. Remote Sens. Environ. 58 (3), 289–298. https://doi.org/10.1016/S0034-4257(96)00072-7.

Gitelson, A.A., Viña, A., Ciganda, V., Rundquist, D.C., Arkebauer, T.J., 2005. Remote estimation of canopy chlorophyll content in crops. Geophys. Res. Lett. 32 (8). https://doi.org/10.1029/2005GL022688.

Gorelick, N., Hancher, M., Dixon, M., Ilyushchenko, S., Thau, D., Moore, R., 2017. Google earth engine: planetary-scale geospatial analysis for everyone. Remote Sens. Environ. 202, 18–27. https://doi.org/10.1016/j.rse.2017.06.031.

Gorodkin, J., 2004. Comparing two K-category assignments by a K-category correlation coefficient. Comput. Biol. Chem. 28 (5), 367–374. https://doi.org/10.1016/j.compbiolchem.2004.09.006.

Huesca, M., Roth, K.L., García, M., Ustin, S.L., 2019. Discrimination of canopy structural types in the Sierra Nevada Mountains in central California. Rem. Sens. 11. https://doi.org/10.3390/rs11091100.

Huete, A.R., 1988. A soil-adjusted vegetation index (SAVI). Remote Sens. Environ. 25 (3), 295–309. https://doi.org/10.1016/0034-4257(88)90106-X.

Huete, A., Justice, C., Liu, H., 1994. Development of vegetation and soil indices for MODIS-EOS. Remote Sens. Environ. 49 (3), 224–234. https://doi.org/10.1016/0034-4257(94)90018-3.

ICONA, 1987. Guía fotográfica para la identificación de modelos de combustible. Madrid: Ministerio de Agricultura, Pesca y Alimentación (MAPA).

IGN, 2016. Base topográfica nacional 1:25.000. Available on the Download Center of the National Geographic Information Center (CNIG): http://centrodedescargas.cnig.es/CentroDescargas. April, 2017.

IGN, 2021. Frecuencia de incendios por término municipal ocurridos entre los años 1996 a 2015. Available on the Nature Data Bank of the Spanish Ministry of Ecological Transition and Demographic Challenge: https://www.miteco.gob.es/es/biodiversidad/servicios/banco-datos-naturaleza/informacion-disponible/incendios-forestales.aspx.

IPCC, 2021. In: Masson-Delmotte, V., Zhai, P., Pirani, A., Connors, S.L., Péan, C., Berger, S., Caud, N., Chen, Y., Goldfarb, L., Gomis, M.I., Huang, M., Leitzell, K., Lonnoy, E., Matthews, J.B.R., Maycock, T.K., Waterfield, T., Yelekçi, O., Yu, R., Zhou, B. (Eds.), Climate Change 2021: the Physical Science Basis. Contribution of Working Group I to the Sixth Assessment Report of the Intergovernmental Panel on Climate Change. Cambridge University Press. (in press).

Jain, P., Coogan, S.C., Subramanian, S.G., Crowley, M., Taylor, S., Flannigan, M.D., 2020. A review of machine learning applications in wildfire science and management. Environ. Rev. 28, 478–505. https://doi.org/10.1139/er-2020-0019.

Kamal, M., Phinn, S., 2011. Hyperspectral data for Mangrove species mapping: a comparison of pixel-based and object-based approach. Rem. Sens. 3 (10), 2222–2242. https://doi.org/10.3390/rs3102222.

Keeley, J.E., Bond, W.J., Bradstock, R.A., Pausas, J.G., Rundel, P.W., 2011. In: Fire in Mediterranean Ecosystems: Ecology, Evolution and Management. Cambridge University Press. https://doi.org/10.1017/CBO9781139033091.

Kingma, D.P., Ba, J., 2017. Adam: a method for stochastic optimization. In: International Conference on Learning Representations. arXiv:1412.6980.

Landis, J.R., Koch, G.G., 1977. The Measurement of observer agreement for categorical data. Biometrics 33 (1), 159–174. https://doi.org/10.2307/2529310.

Lecun, Y., Bottou, L., Bengio, Y., Haffner, P., 1998. Gradient-based learning applied to document recognition. Proc. IEEE 86, 2278–2324. https://doi.org/10.1109/5.726791.

Libertà, G., Pfeiffer, H., Artés Vivancos, T., Grecchi, R., San-Miguel-Ayanz, J., Branco, A., Tomàs Rigo, D., Nuijten, D., Durrant, T., Onida, M., Löffler, P., Ferrari, D., Boca, R., Maianti, P., Oom, D., European Commission, Joint Research Centre. Forest fires in Europe, Middle East and North Africa 2020. In: Technical Report. EUR 30862 EN. Institute for Environment and Sustainability. Joint Research Centre. European Commission LU. https://data.europa.eu/doi/10.2760/059331.

Maas, A.L., Hannun, A.Y., Ng, A.Y., 2013. Rectifier nonlinearities improve neural network acoustic models. In: ICML Workshop on Deep Learning for Audio, Speech and Language Processing.

Marino, E., Ranz, P., Tomé, J.L., Noriega, M.A., Esteban, J., Madrigal, J., 2016. Generation of high-resolution fuel model maps from discrete airborne laser scanner and Landsat-8 OLI: a low-cost and highly updated methodology for large areas. Remote Sens. Environ. 187, 267–280. https://doi.org/10.1016/j.rse.2016.10.020.

Maxwell, S.K., Schmidt, G.L., Storey, J.C., 2007. A multi-scale segmentation approach to filling gaps in Landsat ETM+ SLC-off images. Int. J. Rem. Sens. 28 (23), 5339–5356. https://doi.org/10.1080/01431160601034902.

Ministry for Ecological Transition and Demographic Challenge, 2022. Estadística general de incendios forestales. Available on the Spanish Ministry for Ecological Transition and Demographic Challenge: https://www.miteco.gob.es/es/biodiversidad/temas/inventarios-nacionales/inventario-espanol-patrimonio-natural-biodiv/sistema-indicadores/06c-estadistica-incendios-forestales.aspx.

Moreira, F., Viedma, O., Arianoutsou, M., Curt, T., Koutsias, N., Rigolot, E., Barbati, A., Corona, P., Vaz, P., Xanthopoulos, G., Mouillot, F., Bilgili, E., 2011. Landscape – wildfire interactions in southern Europe: implications for landscape management. J. Environ. Manag. 92 (10), 2389–2402. https://doi.org/10.1016/j.jenvman.2011.06.028.

Myint, S.W., Gober, P., Brazel, A., Grossman-Clarke, S., Weng, Q., 2011. Per-pixel vs. object-based classification of urban land cover extraction using high spatial resolution imagery. Remote Sens. Environ. 115, 1145–1161. https://doi.org/10.1016/j.rse.2010.12.017.

Nair, V., Hinton, G.E., 2010. Rectified linear units improve restricted Boltzmann machines. In: Proceedings of the 27th International Conference on International Conference on Machine Learning ICML'10. Omnipress, Madison, WI, USA, pp. 807–814.

NASA LP DAAC, 2015. ASTER level 1 precision terrain corrected registered at-sensor radiance V003 [data set]. NASA EOSDIS land processes DAAC. Last accessed: September 2021 from. https://doi.org/10.5067/ASTER/AST_L1T.003.

NASA, J.P.L., 2020. NASADEM Merged DEM Global 1 arc second V001. In: NASA EOSDIS Land Processes DAAC. Last accessed: September 2021 from. https://doi.org/10.5067/MEaSUREs/NASADEM/NASADEM_HGT.001.

Navarro-Carrión, J.T., León-Cadena, P., Ramon-Morte, A., 2021. Open data repositories and Geo Small Data for mapping the wildfire risk exposure in wildland urban interface (WUI) in Spain: a case study in the Valencian Region. Remote Sens. Appl.: Soc. Environ. 22, 100500. https://doi.org/10.1016/j.rsase.2021.100500.

Prieto-Herráez, D., Asensio, M.I., Ferragut, L., Cascón, J.M., Morillo, A., 2017. A GIS-based fire spread simulator integrating a simplified physical wildland fire model and a wind field model. Int. J. Geogr. Inf. Sci. 31 (11), 2142–2163. https://doi.org/10.1080/13658816.2017.1334889.

Pu, R., Gong, P., Yu, Q., 2008. Comparative analysis of EO-1 ALI and hyperion, and Landsat ETM+ data for mapping forest crown closure and leaf area index. Sensors 8 (6), 3744–3766. https://doi.org/10.3390/s8063744.

Riaño, D., Chuvieco, E., Salas, J., Palacios-Orueta, A., Bastarrika, A., 2002. Generation of fuel type maps from Landsat TM images and ancillary data in Mediterranean ecosystems. Can. J. For. Res. 32, 1301–1315. https://doi.org/10.1139/x02-052.

Rogers, A.S., Kearney, M.S., 2004. Reducing signature variability in unmixing coastal marsh Thematic Mapper scenes using spectral indices. Int. J. Rem. Sens. 25 (12), 2317–2335. https://doi.org/10.1080/01431160310001618103.

Rothermel, R.C., 1972. In: A Mathematical Model for Predicting Fire Spread in Wildland Fuels. Research Paper INT-115 U.S. Department of Agriculture, Intermountain Forest and Range Experiment Station. https://www.fs.usda.gov/treesearch/pubs/32533.

Ruiz, L.A., Recio, J.A., Crespo-Peremarch, P., Sapena, M., 2018. An object-based approach for mapping forest structural types based on low-density LiDAR and multispectral imagery. Geocarto Int. 33, 443–457. https://doi.org/10.1080/10106049.2016.1265595.

Schmidt, G., Jenkerson, C., Masek, J., Vermote, E., Gao, F., 2013. Landsat ecosystem disturbance adaptive processing system (LEDAPS) algorithm description. In: U.S. Geological Survey Open-File Report USGS. Series: Open-File Report 2013-1057. https://doi.org/10.3133/ofr20131057.

Shao, S., Wang, P., Yan, R., 2019. Generative adversarial networks for data augmentation in machine fault diagnosis. Comput. Ind. 106, 85–93. https://doi.org/10.1016/j.compind.2019.01.001.

Silleos, N.G., Alexandridis, T.K., Gitas, I.Z., Perakis, K., 2006. Vegetation indices: advances made in biomass estimation and vegetation monitoring in the last 30 years. Geocarto Int. 21 (4), 21–28. https://doi.org/10.1080/10106040608542399.

Singh, M., Tyagi, K.D., 2021. Pixel based classification for Landsat 8 OLI multispectral satellite images using deep learning neural network. Remote Sens. Appl.: Soc. Environ. 24, 100645. https://doi.org/10.1016/j.rsase.2021.100645.

Srivastava, N., Hinton, G., Krizhevsky, A., Sutskever, I., Salakhutdinov, R., 2014. Dropout: a simple way to prevent neural networks from overfitting. J. Mach. Learn. Res. 15 (56), 1929–1958. http://jmlr.org/papers/v15/srivastava14a.html.

Stavros, E.N., Coen, J., Peterson, B., Singh, H., Kennedy, K., Ramirez, C., Schimel, D., 2018. Use of imaging spectroscopy and LIDAR to characterize fuels for fire behavior prediction. Remote Sens. Appl.: Soc. Environ. 11, 41–50. https://doi.org/10.1016/j.rsase.2018.04.010.

Stephenson, C., Handmer, J., Betts, R., 2013. Estimating the economic, social and environmental impacts of wildfires in Australia. Environ. Hazards 12 (2), 93–111. https://doi.org/10.1080/17477891.2012.703490.

Sullivan, A.L., 2009a. Wildland surface fire spread modelling, 1990–2007. 1: physical and quasi-physical models. Int. J. Wildland Fire 18, 349–368. https://doi.org/10.1071/WF06143.

Sullivan, A.L., 2009b. Wildland surface fire spread modelling, 1990–2007. 2: empirical and quasi-empirical models. Int. J. Wildland Fire 18, 369–386. https://doi.org/10.1071/WF06142.

Sullivan, A.L., 2009c. Wildland surface fire spread modelling, 1990–2007. 3: simulation and mathematical analogue models. Int. J. Wildland Fire 18, 387–403. https://

doi.org/10.1071/WF06144.

Szpakowski, D.M., Jensen, J.L.R., 2019. A review of the applications of remote sensing in fire ecology. Rem. Sens. 11. https://doi.org/10.3390/rs11222638.

Tragsatec, 2022. https://www.tragsa.es/en/the-group/companies/Paginas/tragsatec.aspx. Jun 2022.

Trucchia, A., Egorova, V., Butenko, A., Kaur, I., Pagnini, G., 2019. RandomFront 2.3: a physical parameterisation of fire spotting for operational fire spread models – implementation in WRF-SFIRE and response analysis with LSFire + . Geosci. Model Dev. (GMD) 12, 69–87. https://doi.org/10.5194/gmd-12-69-2019.

Tucker, C.J., 1979. Red and photographic infrared linear combinations for monitoring vegetation. Remote Sens. Environ. 8 (2), 127–150. https://doi.org/10.1016/0034-4257(79)90013-0.

USGS. LANDSAT/LE07/C01/T1_sr. Landsat-7 Data set courtesy of the U.S. Geological Survey. Accessed from: https://developers.google.com/earth-engine/datasets/catalog/LANDSAT_LE07_C01_T1_SR.

Wan, Z., Hook, S., Hulley, G., 2015. MOD11A1 MODIS/Terra Land Surface Temperature/Emissivity Daily L3 Global 1km SIN Grid V006 [Data Set]. NASA EOSDIS Land Processes DAAC. Last accessed: September 2021. https://doi.org/10.5067/MODIS/MOD11A1.006.

Waske, B., Benediktsson, J., Sveinsson, J., 2009. Classifying remote sensing data with support vector machines and imbalanced training data. In: Benediktsson, J.A., Kittler, J., Roli, F. (Eds.), Multiple Classifier Systems. Springer Berlin Heidelberg, pp. 375–384.

Yin, G., Mariethoz, G., McCabe, M.F., 2017. Gap-Filling of Landsat 7 imagery using the direct sampling method. Rem. Sens. 9 (1). https://doi.org/10.3390/rs9010012.

Zhang, C., Sargent, I., Pan, X., Li, H., Gardiner, A., Hare, J., Atkinson, P.M., 2019. Joint Deep Learning for land cover and land use classification. Remote Sens. Environ. 221, 173–187. https://doi.org/10.1016/j.rse.2018.11.014.

Zhang, G., Wang, M., Liu, K., 2021. Deep neural networks for global wildfire susceptibility modelling. Ecol. Indicat. 127, 107735. https://doi.org/10.1016/j.ecolind.2021.107735.